Journal of Surgical Research **82,** 275–284 (1999)
Article ID jsre.1998.5555, available online at http://www.idealibrary.com on IDEAL®

High-Resolution Optical Coherence Tomography-Guided Laser Ablation of Surgical Tissue[1]

Stephen A. Boppart, Ph.D.,*,†,[2] Juergen Herrmann, Ph.D.,* Costas Pitris, M.S.E.E.,*,†
Debra L. Stamper, Ph.D.,‡ Mark E. Brezinski, M.D., Ph.D.,§ and James G. Fujimoto, Ph.D.*

**Department of Electrical Engineering and Computer Science, Research Laboratory of Electronics, and †Harvard–MIT Division of Health Sciences and Technology, Massachusetts Institute of Technology, Cambridge, Massachusetts 02139; ‡Department of Biology, King's College, Wilkes-Barre, Pennsylvania 18711; and §Cardiac Unit, Harvard Medical School, Massachusetts General Hospital, Boston, Massachusetts 02114*

Submitted for publication September 17, 1998

Background. **Optical coherence tomography (OCT) is a compact high-speed imaging technology which uses infrared light to acquire cross-sectional images of tissue on the micrometer scale. Because OCT images are based on the optical backscattering properties of tissue, changes in tissue optical properties due to surgical laser ablation should be detectable using this technique. In this work, we examine the feasibility of using real-time OCT imaging to guide the placement and observe the dynamics of surgical laser ablation in a variety of tissue types.**

Materials and methods. **More than 65 sites on five *ex vivo* rat organ tissue types were imaged at eight frames per second before, during, and after laser ablation. Ablation was performed with a coincident continuous wave argon laser operating at 514-nm wavelength and varying exposure powers and durations. Following imaging, tissue registration was achieved using microinjections of dye followed by routine histologic processing to confirm the morphology of the ablation site.**

Results. **High-speed OCT imaging at eight frames per second permitted rapid tissue orientation and guided ablation in numerous organ specimens. Acquisition rates were fast enough to capture dynamic changes in optical backscatter which corresponded to thermal tissue damage during laser ablation.**

Conclusions. **The ability of high-resolution high-speed OCT to guide laser ablation and image the dynamic changes suggests a role in image-guided surgical procedures, such as the ablation of neoplasms. Future *in vivo* studies are necessary to demonstrate performance intraoperatively.**

Key Words: **laser surgery; imaging; ablation; neoplasia; tumor.**

INTRODUCTION

The surgical laser has been effective in the surgical suite because it provides a cutting and coagulation tool with controllable powers, a compact, flexible fiber-optic delivery system, and wavelength- and tissue-specific cutting efficiencies [1, 2]. Lasers are becoming standard instruments for the ablation of endometrial foci of the reproductive tract [3], interstitial laser ablation of tumors [4], and surgical ophthalmologic procedures [5, 6]. While laser use has been widespread, control and dosimetry of the delivery of laser radiation have relied largely on visual feedback of the surface ablation site. This is a limitation which, by not allowing full visualization of the location and extent of subsurface tissue ablation, has the potential to result in iatrogenic injury.

Advancements in high-resolution image-guidance technologies coupled with the ability to tightly focus a laser beam would permit precise ablation of tissue, such as a neoplasm, while minimizing collateral injury.

[1] This research is supported in part by the Medical Free Electron Laser Program, Office of Naval Research Contract N000014-97-1-1066; the National Institutes of Health, Contracts NIH-9-RO1-CA75289-01, NIH-9-RO1-EY11289-13 (J.G.F.), NIH-RO1-AR44812-01 (M.E.B.), and NIH-1-R29-HL55686-01A1 (M.E.B.); the Whittaker Foundation Contract 96-0205 (M.E.B.); Air Force Office of Scientific Research Contract F49620-98-1-0139; and the Air Force Palace Knight Program (S.A.B.).

[2] To whom correspondence should be addressed at Department of Electrical Engineering and Computer Science, Research Laboratory of Electronics, Harvard–MIT Division of Health Sciences and Technology, Massachusetts Institute of Technology, 77 Massachusetts Ave., Room 36-345, Cambridge, MA 02139. Fax: (617) 253-9611. E-mail: boppart@mit.edu.

0022-4804/99 $30.00

Currently, however, no intraoperative imaging technique exists with sufficient resolution to guide the placement and fast acquisition rates to image the dynamics of surgical laser ablation. Magnetic resonance imaging and computed tomography can image whole body and organs, but have resolutions between 500 μm and 1 mm, insufficient to resolve tissue microstructure. In addition, their use for high-speed intraoperative image guidance is limited by size, cost, and complexity [7]. Ultrasound imaging can be performed intraoperatively, either noninvasively or with endoscopic ultrasound probes, but resolutions are typically no higher than 100 μm and physical contact or an index-matching medium is required [8]. A compact, high-resolution, high-speed imaging technique capable of monitoring tissue coagulation, cutting, and ablation intraoperatively at a localized site would permit image-guided surgical laser procedures to be monitored for controlled therapy and subsequent reduction in iatrogenic injury.

Optical coherence tomography (OCT)[3] is a recently developed micron-scale, real-time imaging technology [9]. OCT is analogous to ultrasound, measuring the intensity of backreflected infrared light rather than acoustic waves. OCT was first applied clinically to image and track retinal diseases in the transparent structures of the human eye [10]. Recently, OCT imaging has been developed for imaging nontransparent tissues [11–13]. Imaging depths are limited to a few millimeters because of optical attenuation due to absorption and scattering; however, these imaging depths are sufficient for many diagnostic applications including performing may types of intraoperative monitoring. Studies have shown the feasibility of using OCT as a surgical diagnostic tool [14] and for intraoperative monitoring of microsurgical anastomoses of vessels and nerves [15]. *In vivo* studies have been performed in an animal model which demonstrate the feasibility of catheter–endoscope-based OCT imaging of internal organ systems including the gastrointestinal and pulmonary tracts [16].

Several features, in addition to high resolution, make OCT attractive for guiding surgical ablation. First, OCT imaging is fiber based, allowing it to be readily integrated with hand-held surgical probes, laparoscopes, catheters, and endoscopes [17]. Second, unlike ultrasound, OCT imaging is noncontact and can be performed through air. Third, OCT systems are compact and portable, an important consideration for the operating suite. Finally, OCT imaging is performed at high speeds, allowing image data to be acquired rapidly over large regions of tissue.

The pathologic effects of laser-induced hyperthermia within biological tissue [18] and the thermal and mechanical effects of laser tissue ablation have been previously analyzed and well characterized [19]. The majority of studies, however, have used histological preparations at single time points to document the tissue changes that occur. Dynamic changes in tissue optical properties have been characterized [20, 21], but have relied on spectroscopic transmission and reflection data rather than image data. OCT has been used to characterize the changes in the retina following laser injury; however, images were acquired at 5-s intervals [22]. In tissues exhibiting birefringence, such as muscle and tendon, polarization-sensitive OCT has been used to detect birefringence changes following thermal heating [23, 24]. Birefringent changes may indicate early thermal injury, but detection is limited to specific tissue types. No studies have been performed using high-speed OCT to image real-time changes in optical backscatter in highly scattering tissues during laser ablation.

In this study, we investigate the feasibility of using high-speed OCT imaging to guide the placement and follow the dynamics of surgical laser ablation. Argon laser ablation at 514 nm, a wavelength frequently used surgically, is performed in five different *ex vivo* rat organs to assess OCT imaging performance and variations between tissue types. The use of OCT to monitor ablative therapy in real time may enable more precise control of laser delivery and a reduction in iatrogenic injury.

MATERIALS AND METHODS

Optical coherence tomography. Optical coherence tomography is a technique for performing high-resolution imaging in biological tissue [9]. OCT is somewhat analogous to ultrasound B-mode imaging except backreflections of light are detected rather than acoustic waves. Whereas ultrasound pulse propagation can be measured electronically, the echo time delay of light used in OCT imaging cannot be measured directly because the velocity of light is extremely high and the resulting echo delays are extremely short. Therefore, in OCT, a technique known as interferometry is used. This technique measures the magnitude and echo time delay of reflected or backscattered light by comparing the reflected light beam to a beam which travels a reference path of known delay.

Figure 1 shows a schematic of the OCT system. The OCT system uses a fiber-optic implementation of a Michelson-type interferometer [9]. A laser or other light source with a broad spectral bandwidth (short coherence length) is coupled into the fiber-optic interferometer and split by a fiber coupler into a sample arm and a reference arm. A high-speed optical delay line is used in the reference arm to vary the optical path length of the reference arm. The optical beam from the sample arm of the interferometer is directed onto the object or specimen to be imaged. Light is backreflected or backscattered from microstructural features internal to the specimen and has a different echo time delay depending on its depth. When the echo time delay of the light from the specimen matches the echo time delay of light traveling the reference path to within the coherence length of the light, interference is detected at the output of the interferometer. The interference is detected by a photodetector and demodulated electronically to give a measurement of the magnitude and echo delay of backscattered light. A pair of steering mirrors controlled by galvanometer actuators is used to scan the OCT imaging beam across the specimen. By measuring the magnitude and echo delay of

[3] Abbreviation used: OCT, optical coherence tomography.

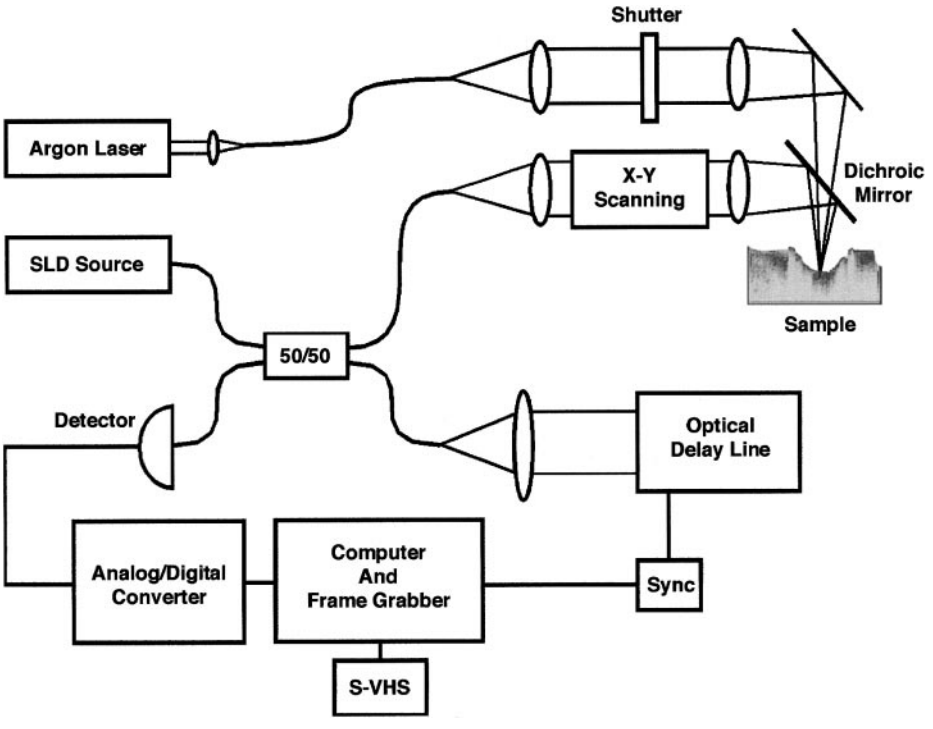

FIG. 1. Optical coherence tomography schematic. OCT uses a fiber-optic interferometer to localize optical backreflections from within tissue. Two- and three-dimensional subsurface images are generated by scanning the beam across the tissue. Images can be acquired at eight frames per second and saved either digitally or to Super-VHS tape. OCT imaging is coincident with a continuous wave argon laser to monitor the dynamic effects of laser tissue ablation. SLD, super-luminescent diode.

backscattered light at different transverse positions on the specimen, a two-dimensional data set is generated which represents the backscattering through a cross-sectional plane of the specimen. This data set is displayed as an image using a gray-scale or false-color representation.

The axial resolution of the imaging is determined by the coherence length of the light source. The coherence length is inversely proportional to the spectral bandwidth; therefore, light sources with a broad spectral bandwidth will enable high resolutions. The studies reported here were performed using a commercially available low-coherent light source which is based on a super-luminescent diode/amplifier (AFC Technologies Inc., Hull, Quebec, Canada). Other sources of low-coherence light can also be used including superluminescent optical fiber sources or short-pulse lasers. The light source used for these experiments had a center wavelength of 1.3 μm and a free space axial resolution of 18 μm. The axial resolution was determined by measuring the point spread function from a mirror placed at the sample position in the OCT apparatus. The transverse resolution was determined by the spot size of the incident beam within the tissue. The spot size was 30 μm which yielded a 1.1-mm confocal parameter (depth of field). The confocal parameter for the beam was selected to closely match axial and transverse resolutions while maintaining a sufficient depth of field.

The signal-to-noise ratio was 115 dB using 5 mW of incident power on the specimen. For typical tissues, this sensitivity permits imaging to depths up to 3 mm. A single axial scan was acquired for every sweep of the optical delay line in the reference arm. For high-speed image acquisition, the length of the axial scan was 3 mm and 256 pixels were acquired during each axial scan, corresponding to an axial pixel sampling distance of 11.7 μm/pixel. Images were generated by assembling adjacent axial scans to form a two-dimensional cross-sectional image of the optical backscatter from within the specimen. A total of 256 axial scans were acquired across a transverse distance of 3 mm, corresponding to a transverse pixel sampling distance of 11.7 μm/pixel. Images were displayed as the logarithm of the backscattered intensity versus position in gray scale on a computer monitor and simultaneously recorded to Super-VHS video tape. The acquisition rate was eight frames per second or 125 ms for each image.

Laser ablation was performed using a continuous wave argon laser operating predominantly at a wavelength of 514 nm. As shown in Fig. 1, 1–3 W of output power from the argon laser was coupled into a fiber and focused to a 0.8-mm-diameter spot on the tissue surface. The argon beam was aligned and centered within the OCT imaging plane. A mechanical shutter was used to control the argon laser exposures on the sample. Prior to laser ablation, each specimen was manipulated under OCT image guidance to locate a relatively uniform region of tissue for the ablation site. During exposures, both the argon beam and the specimen remained stationary. This setup permitted image acquisition immediately prior to and after exposure to track the optical changes occurring within the tissue during laser ablation.

Specimen preparation and imaging. Sprague–Dawley rats were euthanized with 42 mg/kg intraperitoneal injections of phenobarbital (Nembutal). Rat organs including brain, liver, kidney, lung, and rectus abdominis muscle were immediately resected, placed in 0.9% saline, and stored at room temperature prior to imaging. More than 65 sites on five *ex vivo* rat organ tissues were OCT imaged. A three-dimensional micron-precision computer-controlled stage was used to position the specimen under the OCT imaging beam and was used to acquire three-dimensional data sets. Argon laser ablation was performed at discrete sites on the organs using varying argon powers and exposure durations. Immediately following image acquisition, the location of the image plane was marked with India ink for registration between OCT images and histology. Specimens were placed in a 10% buffered solution of formalin for standard histological preparation. Histological sections, 5 μm thick, were sectioned

and stained with hematoxylin and eosin for comparison with acquired OCT images. The protocol for the care and handling of animals used in this study has been approved by the Massachusetts Institute of Technology Committee on Animal Care.

RESULTS

Before performing dynamic imaging studies, a single ablation site was imaged and thoroughly investigated to determine what optical changes within tissue, following laser ablation, were detectable with OCT. A 10-s, 3-W argon laser exposure was used to form an ablation crater in rat rectus abdominis muscle. The specimen was then translated on a multiaxis translational stage to perform 3-D imaging of the crater. Sixty cross-sectional images were acquired at 100-μm intervals to produce a 3-D data set. One projection from this data set is shown in Fig. 2A. The deep crater can be seen in the center of the projection. Surrounding the crater is an elevated region of damage which decreases radially outward from the center.

A sequence of cross-sectional images from this data set is shown in Fig. 2B. These provide information on the depth- and distance-dependent distribution of the thermal energy. The number in each image refers to the distance from the center of the crater at which the cross-sectional image was acquired. At a distance of 3.75 mm from the center, small distortions in the muscle layers (arrow) are observed, although little change has occurred at the tissue surface. At 3.0 mm, thermal injury has elevated the tissue surface and distorted an internal low-backscattering layer. At 2.25 mm, a region of increased optical backscatter has appeared. This region appears deeper in the 1.5-mm section. At 0.75 mm from the crater center, carbonization of the tissue results in significant shadowing of underlying structures. A cross-section through the center of the crater is shown in the last image. The vertical bands of low backscatter adjacent to the crater are due to shadowing by the vertical crater walls which are lined with carbonized tissue. Carbonized tissue scatters and absorbs the incident light, decreasing imaging penetration.

Surrounding the deep crater in Fig. 2A lie concentric rings of tissue damage. These are the result of a radial thermal distribution outward from the site of the incident beam. The differences between each ring are likely the result of different thermal damage mechanisms, if one assumes the tissue is homogeneous. To optimally assess these radial distributions, the 3-D data set is resectioned in the *en face* plane, as would be viewed from the surface and with increasing depth into the tissue. Resectioned slices are shown in Fig. 2C. The number in each figure refers to the depth of the reconstructed plane from the surface. The shallow planes (150–600 μm) show some empty spaces (lower white regions) because the axes of the tissue block were not exactly orthogonal to the translation stage axes. The image at 150 μm shows a relatively uniform ring consistent with the elevated region appearing in the 3-D projection of Fig. 2A. At greater depths (450–900 μm), however, a multiple-ring pattern is evident, possibly indicating different zones of tissue damage. An alternative explanation may be a concentric elevation of birefringent tissue layers presenting as regions of low and high optical backscatter. At a depth of 1350 μm, the crater bottom is approached and the concentric rings have diminished. At 1500 μm, the region of high backscatter in the center represents tissue immediately below the crater bottom and the white ring of reduced optical backscatter is due to the attenuation of the incident beam by the carbonized tissue lining the nearly vertical crater walls.

Ablation dynamics represented as changes in optical backscatter within the OCT images are shown in the remaining figures. Figure 3 is an image sequence showing thermal injury in kidney tissue from 1-W, 3-s argon laser exposure. The OCT images illustrate the relatively homogeneous nature of the outer cortex of the kidney. Imaging penetration in this tissue is limited to $\approx$1 mm. An increased region of optical backscatter is first observed at 0.1 s. This is followed by an outward propagating front of increased backscatter shown at 0.6 s. A region of low backscatter develops at the center of the lesion (1.6 s). Backscatter from this region then increases over time (3.0 s). This exposure was below the threshold for surface membrane rupture, tissue ejection, and crater formation. Based on empirical ablation observations, membrane rupture would likely have occurred within the following second if the exposure had continued. OCT image guidance and feedback enabled laser exposure to be terminated immediately prior to membrane rupture. The corresponding histology is also shown, indicating a region of coagulated tissue (arrows) with no tissue fragmentation.

The ablation threshold at which tissue is ejected is documented by a sequence of images showing thermal injury in rat liver. A superthreshold ablation sequence with corresponding histology is shown in Fig. 4. The exposure is allowed to continue for 6 s, resulting in ejection of tissue and crater formation. The changes in optical backscatter observed prior to membrane rupture are similar to those observed for the subthreshold exposure in Fig. 3. The superthreshold histology shows marked tissue ablation and fragmentation within the lesion crater. Below the crater extends a zone of coagulated tissue (arrows) which is not fully imaged with OCT due to the poor imaging penetration through the carbonized crater wall.

In contrast to the ablation of tissues such as liver and kidney which have a high absorption coefficient at argon laser wavelengths, Fig. 5 shows the ablation of brain tissue. The lower absorption coefficient implies

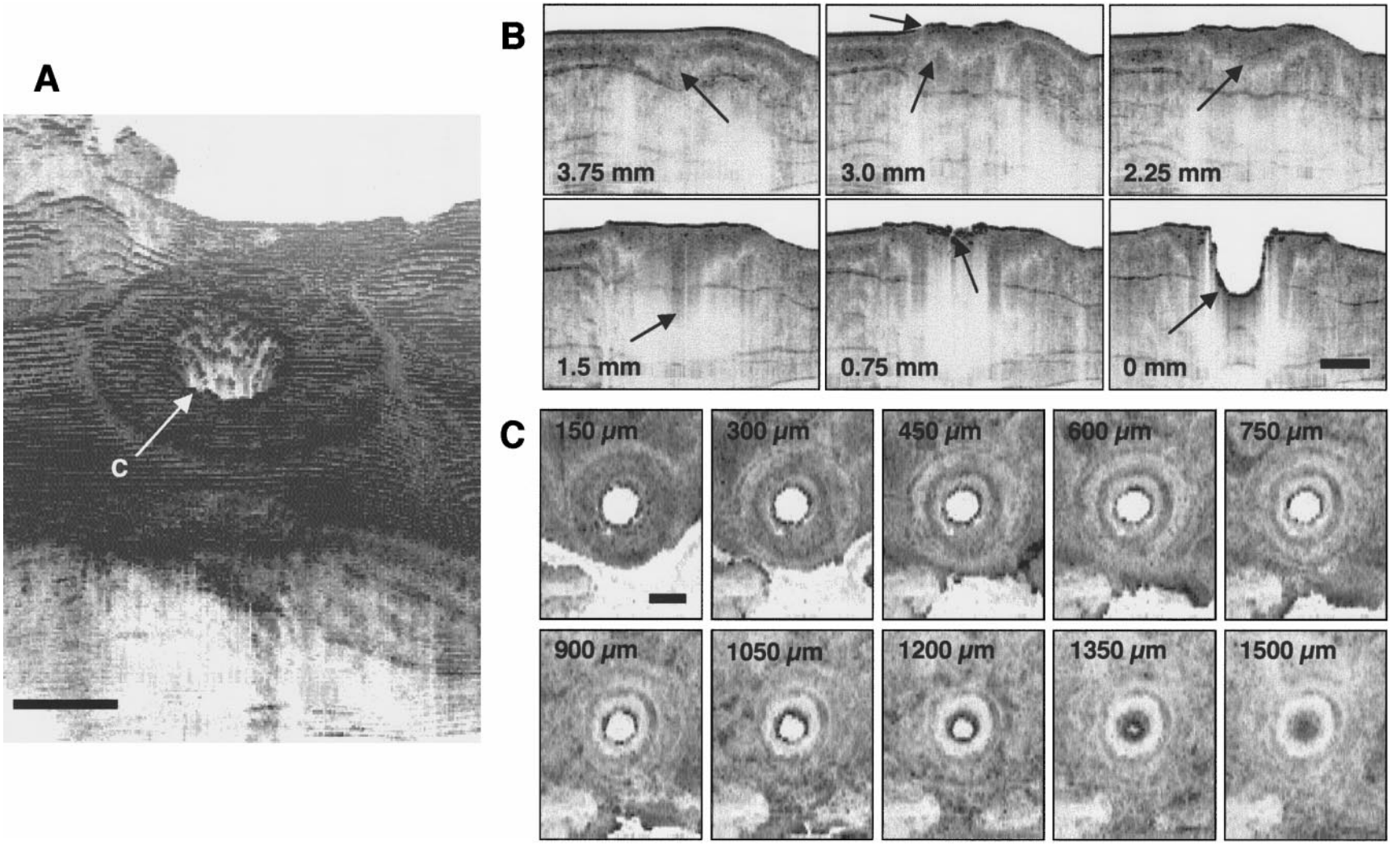

FIG. 2. Laser ablation crater. Three-dimensional projection and resectioned data sets are shown for a 3-W, 10-s argon exposure of rat rectus abdominis muscle. (A) 3-D projection illustrates central ablation crater (c) and concentric zones of thermal injury. (B) Cross-sections through crater. Numbers refer to distance from crater center. Arrows indicate features described in text. (C) *En face* sections in depth illustrate concentric zones of damage. Numbers refer to depth below surface. Bar represents 1 mm.

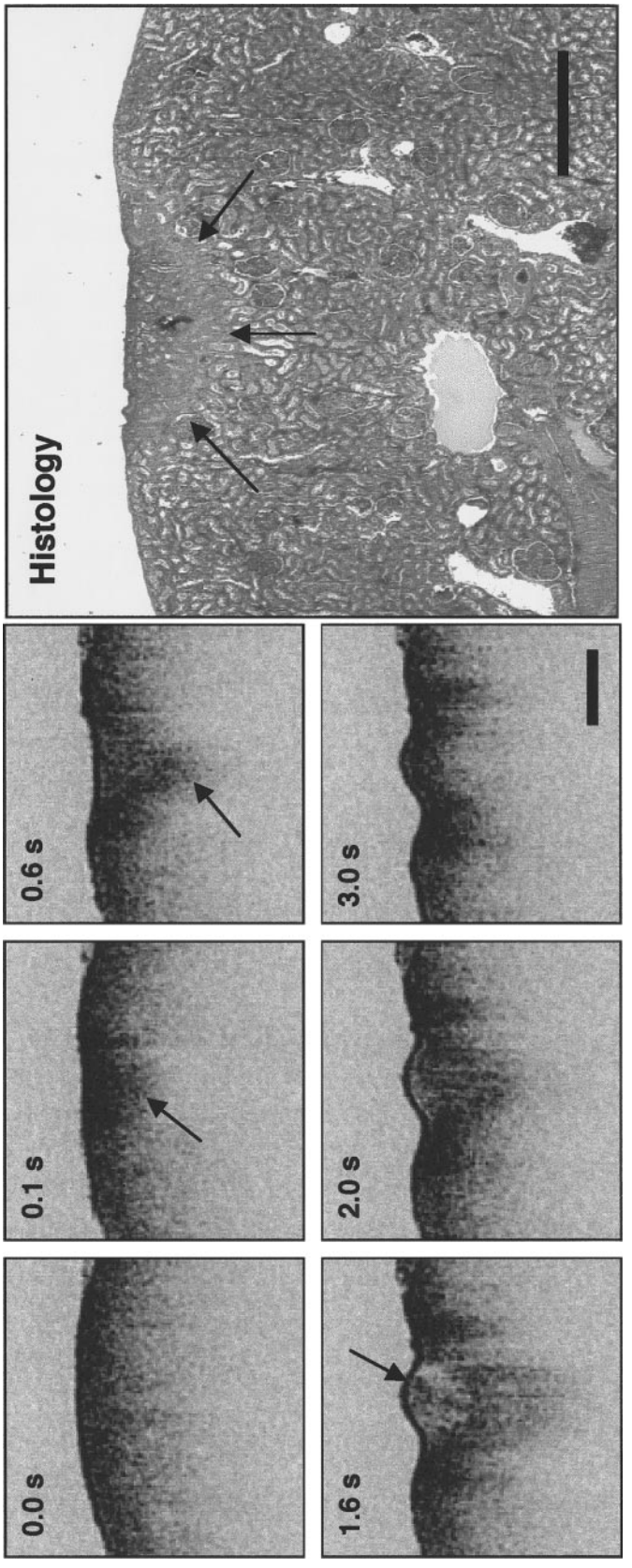

FIG. 3. Kidney ablation. Ablation sequence from 1-W, 3-s argon exposure without surface membrane rupture. OCT image feedback permitted exposure to be halted immediately prior to membrane rupture and crater formation. Optical changes detected with OCT correspond to thermal damage shown in corresponding histology. Arrows indicate features described in text. Bar represents 1 mm.

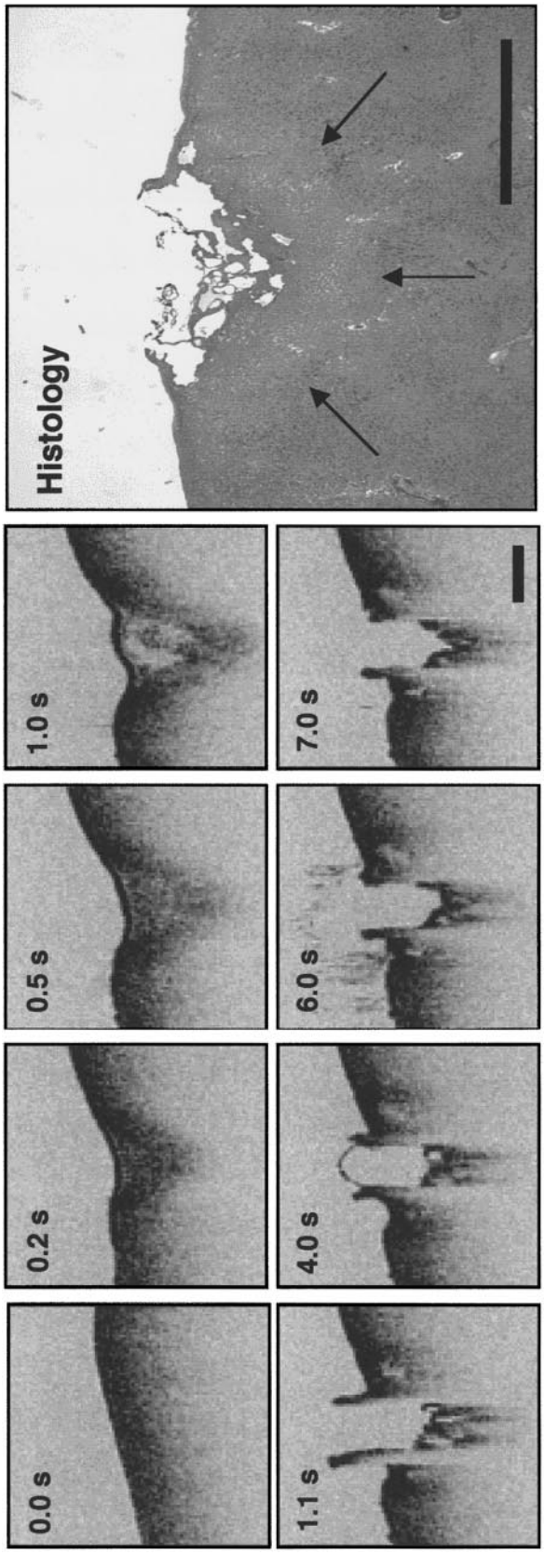

FIG. 4. Liver ablation. Ablation sequence from 1-W, 7-s argon exposure resulting in ejection of tissue. Under OCT image guidance, exposure was continued during submembrane tissue vacuolization, membrane rupture, and crater formation. The corresponding histology confirms that tissue was ejected and that thermal injury surrounds the ablation crater (arrows). Bar represents 1 mm.

that longer exposure durations are required for the same incident power to produce similar effects. This trend was observed for 1 W incident on brain tissue for 20 s. In this sequence, significant vacuolization and tissue heating occur (5.5–13 s) before the surface membrane is ruptured at 14 s. Membrane rupture is followed by ejection of tissue from the lesion, evolution of a smoke plume (16–17 s), and crater formation (20 s).

Figure 6 shows the ablation of lung tissue. Inflated air-filled alveolar spaces represent a large portion of the tissue space making this tissue more inhomogeneous compared to previous specimens. A 1-s exposure of 1-W argon collapses most of the alveoli (0.5–1.0 s) resulting in the rapid deflation of the lung followed by the formation of a shallow crater.

DISCUSSION

We have demonstrated the use of high-speed, real-time OCT imaging for guiding the placement and monitoring the dynamic changes of surgical laser ablation in a variety of tissues. OCT performs high-resolution, cross-sectional imaging and also gives information on the optical scattering properties of tissue. Reflections and optical backscattering occur in tissue due to differences in index of refraction and organization of tissue microstructure including architectural morphology and cellular and subcellular organization. OCT can accurately monitor distributions of ablative damage because the thermal injury disrupts the normal optical properties of the tissue. These changes were illustrated in Fig. 2. In Fig. 2B, the left side of the image at 3.75 mm shows normal rectus abdominis muscle. The layered structure of the muscle is disrupted near the ablation site and replaced by a more homogeneous region. The concentric rings of tissue damage in Fig. 2C show interesting patterns corresponding to the radial distribution of thermal energy, whereas normal tissue would show a relatively homogeneous pattern at each depth.

Carbonization at the surface of the tissue is an undesirable effect which hinders controlled surgical ablation. This effect also represents a limitation for OCT imaging. The high temperatures char tissue, creating a carbonized layer at the surface which rapidly absorbs and scatters both the incident argon and OCT imaging beams. Because of this, OCT imaging penetration is reduced and shadowing artifacts, identified by vertical low-backscattering streaks, appear in the images (Fig. 2B, 0 mm). Fortunately, tissue carbonization is limited to applications of continuous high-power irradiation and studies have identified laser parameters and operative procedures to reduce this effect [25].

The tissue response to thermal injury is highly dependent on the wavelength of the incident light and the tissue absorption coefficient. We have demonstrated OCT imaging in a variety of tissue types to illustrate

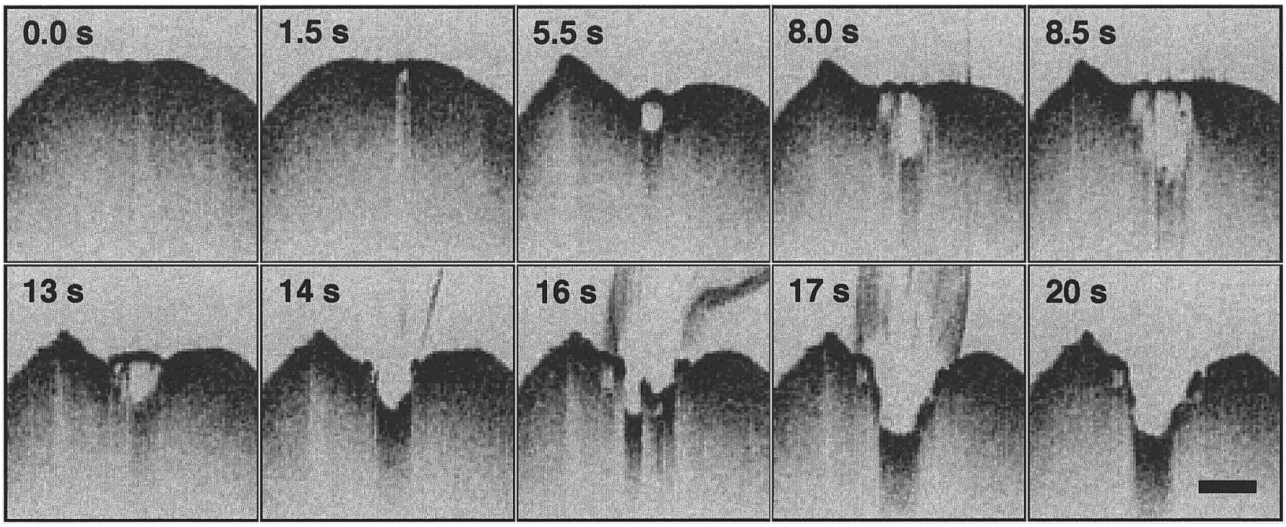

FIG. 5. Brain ablation. Ablation sequence from 1-W, 20-s argon exposure. The lower absorption coefficient of brain tissue compared to hemoglobin-rich tissue such as liver and kidney results in longer exposures required to produce equivalent tissue ablation. Sequence illustrates subsurface tissue vacuolization followed by membrane rupture and tissue ejection. Bar represents 1 mm.

this effect. Hemoglobin is one of the dominant absorbers of visible wavelengths in biological tissue [26]. For the same incident argon power (1 W), the hemoglobin-rich rat liver and kidney (absorption coefficients μ_a = 12 and 1.21 cm^{-1}, respectively) exhibited vacuolization, ablation, and surface membrane rupture within 1–3 s compared to 14 s for brain tissue (μ_a = 0.19 cm^{-1}). This is important clinically because often it is difficult to predict the tissue response to incident laser radiation. Absorption and scattering coefficients, which vary between tissue types, will vary the efficiency of laser ablation. The use of OCT imaging in Fig. 3 provided

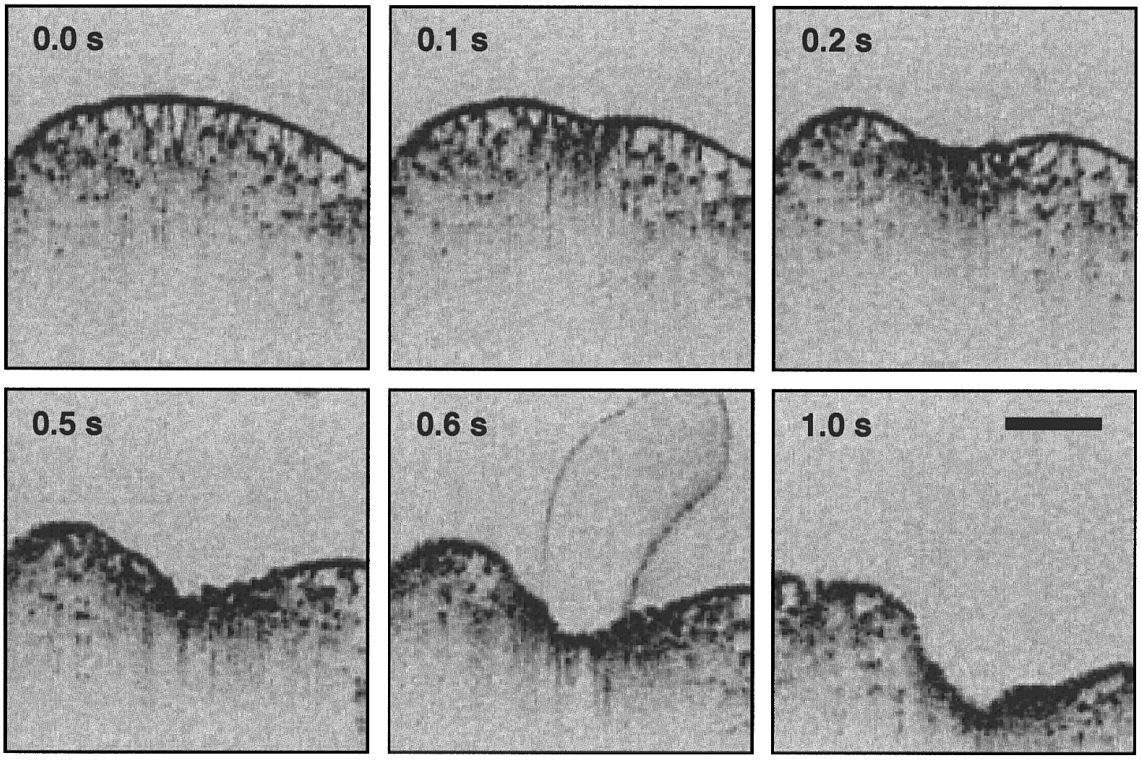

FIG. 6. Lung ablation. Ablation sequence from 1-W, 1-s argon exposure. Air-filled alveoli spaces are clearly evident demonstrating morphological differences from more solid organs. Thermal laser ablation rapidly coagulates lung tissue and deflates alveolar spaces. Bar represents 1 mm.

feedback to terminate laser ablation prior to membrane rupture and tissue ejection, demonstrating the ability to monitor tissue response during laser ablation.

The resolutions of OCT are sufficient to resolve changes in optical backscatter and identify regions of ablated tissue. However, the kidney, liver, and brain specimens appear relatively homogeneous at the current resolutions of OCT. Improvements in resolution will improve the ability to identify tissue microstructure and detect more subtle thermal damage in these tissues. The axial and transverse resolutions in OCT are independent. The axial resolution is inversely proportional to the bandwidth of the optical source. Hence, larger spectral bandwidths can improve axial resolution. Axial resolutions as high as 1.9 μm have been achieved using broader bandwidth laser sources at shorter wavelengths near 800 nm [27, 28]. Shorter wavelengths, however, are absorbed and scattered more in biological tissue, resulting in decreased imaging penetration. The transverse resolution is determined by the beam-focusing optics. Higher transverse resolutions are possible, but at the expense of decreased depth of field. New laser sources and image-processing techniques for improving imaging resolution are topics of active investigation.

The eight frames per second acquisition rate used in this study was sufficient to image the dynamic changes during thermal ablation. More rapid events, such as membrane rupture and tissue ejection, occurred on time scales too fast for OCT imaging. Still, OCT has utility for image guidance of faster processes because OCT can image the integrated effects of ablation. It is not surgically important to capture explosive or disruptive effects on faster time scales as long as the resultant effects can be accurately monitored. Nonetheless, OCT imaging at faster rates is interesting for investigational purposes. Video rate acquisition (30 fps) is possible by either reducing the image size or scanning the optical delay line faster. A resonant scanner can be incorporated into the delay line; however, the nonlinear sinusoidal output would require real-time signal and image processing to correct the images.

The use of an argon laser for surgical ablation is only representative of a broad range of interventional techniques that can be guided using OCT. The 514-nm wavelength of the argon laser is close to the 532-nm wavelength frequently used for tissue cutting and coagulation during surgery and is readily absorbed in tissue. In principle, OCT can be used with other surgical laser wavelengths and with both pulsed and continuous wave laser systems. Because these techniques are optic based, there is potential for integration into a single system with coincident beams for imaging and surgery. In addition, the fiber-optic-based design of OCT allows compact delivery and permits OCT imaging to be integrated with scalpels, scissors, and biopsy forceps. Real-time OCT imaging with these integrated devices could be used to guide the operator in order to avoid injury to sensitive tissue structures such as adjacent nerves, to differentiate tissue or tumor boundaries, or to guide the operator toward specific morphologies. These integrated systems are currently under investigation.

OCT guidance during surgical interventions has a wide range of application across surgical specialties. Because of the micron-scale resolutions afforded by OCT, not only surgical image guidance, but also intraoperative diagnostics of surgical tissue without having to physically resect or biopsy specimens may be possible. Neurosurgery and cardiovascular surgery are two specialties where OCT may be most helpful [29]. Identification and surgical treatment of pathologies must be performed with minimal tissue resection, sparing sensitive adjacent tissue. The single optical fiber delivery of the OCT beam is suitable for integration with minimally invasive techniques. Fiber-based OCT imaging may be possible at physically restrictive sites frequently encountered in the head and neck, the lower respiratory tract, the fallopian tubes, and within the vascular system [30].

In conclusion, these results demonstrate the ability of high-resolution, high-speed OCT to guide the placement of laser ablation sites and image the dynamic changes that occur during thermal tissue ablation. These results suggest that OCT may play a role in image-guided surgical procedures. Future *in vivo* studies are necessary to demonstrate the performance of OCT during intraoperative scenarios.

ACKNOWLEDGMENTS

Dr. Juergen Herrmann was visiting from the University of Erlangen. The authors thank Drs. Brett E. Bouma and Gary J. Tearney of the Wellman Laboratory of Photomedicine, Massachusetts General Hospital, for their technical input. We greatly appreciate the assistance of Ms. Christine Jesser of Massachusetts General Hospital and Ms. Jennifer Libus of King's College for handling tissue specimens and Ms. Cindy Kopf for her assistance in the preparation of the manuscript.

REFERENCES

1. Minton, J. P. The laser in surgery. A 23 year perspective. *Am. J. Surg.* **151:** 725, 1986.
2. Talamo, J. H. *Laser Surgery.* Philadelphia: Lippincott-Raven, 1996.
3. Keye, W. R., Jr., Hansen, L. W., Astin, M., and Poulson, A. M., Jr. Argon laser therapy of endometriosis: A review of 92 consecutive patients. *Fertil. Steril.* **47:** 208, 1987.
4. Dowlatshahi, K., Babich, D., Bangert, J. D., and Kluiber, R. Histological evaluation of rat mammary tumor necrosis by interstitial Nd:YAG laser hyperthermia. *Lasers Surg. Med.* **12:** 159, 1992.
5. Pollack, A., Milstein, A., Oliver, M., and Zalish, M. Circumfer-

ential argon laser photocoagulation for prevention of retinal detachment. *Eye* **8:** 419, 1994.

6. Lin, C. P., Weaver, Y. K., Birngruber, R., Fujimoto, J. G., and Puliafito, C. A. Intraocular microsurgery with a picosecond Nd:YAG laser. *Lasers Surg. Med.* **15:** 44, 1994.
7. Black, M. P., Moriarty, T., Alexander, E., Stieg, P., Woodard, E. J., Gleason, P. L., Martin, C. H., Kikinis, R., Schwartz, R. B., and Jolesz, F. A. Development and implementation of intraoperative magnetic resonance imaging and its neurosurgical applications. *Neurosurgery* **41:** 831, 1997.
8. Goldberg, B. B., Liu, J-B., Merton, D. A., Feld, R. I., Miller, L. S., Cohn, H. E., Barbot, D., Gillum, D. R., Vernick, J. J., and Winkel, C. A. Sonographically guided laparoscopy and mediastinoscopy using miniature catheter-based transducers. *J. Ultrasound Med.* **12:** 49, 1993.
9. Huang, D., Swanson, E. A., Lin, C. P., Schuman, J. S., Stinson, W. G., Chang, W., Hee, M. R., Flotte, T., Gregory, K., Puliafito, C. A., and Fujimoto, J. G. Optical coherence tomography. *Science* **254:** 1178, 1991.
10. Puliatifo, C. A., Hee, M. R., Schumann, J. S., and Fujimoto, J. G. *Optical Coherence Tomography of Ocular Diseases.* Thorofare, NJ: SLACK Inc., 1995.
11. Schmitt, J. M., Yadlowsky, M., and Bonner, R. F. Subsurface imaging of living skin with optical coherence microscopy. *Dermatology* **191:** 9, 1995.
12. Brezinski, M. E., Tearney, G. J., Bouma, B. E., Izatt, J. A., Hee, M. R., Swanson, E. A., Southern, J. F., and Fujimoto, J. G. Optical coherence tomography for optical biopsy: Properties and demonstration of vascular pathology. *Circulation* **93:** 1206, 1996.
13. Fujimoto, J. G., Brezinski, M. E., Tearney, G. J., Boppart, S. A., Bouma, B. E., Hee, M. R., Southern, J. F., and Swanson, E. A. Biomedical imaging and optical biopsy using optical coherence tomography. *Nature Med.* **1:** 970, 1995.
14. Brezinski, M. E., Tearney, G. J., Boppart, S. A., Swanson, E. A., Southern, J. F., and Fujimoto, J. G. Optical biopsy with optical coherence tomography: Feasibility for surgical diagnostics. *J. Surg. Res.* **71:** 32, 1997.
15. Boppart, S. A., Bouma, B. E., Pitris, C., Tearney, G. J., Southern, J. F., Brezinski, M. E., and Fujimoto, J. G. Intraoperative assessment of microsurgery with three-dimensional optical coherence tomography. *Radiology* **208:** 81, 1998.
16. Tearney, G. J., Brezinski, M. E., Bouma, B. E., Boppart, S. A., Pitris, C., Southern, J. F., and Fujitmoto, J. G. *In vivo* endoscopic optical biopsy with optical coherence tomography. *Science* **276:** 2037, 1997.
17. Boppart, S. A., Bouma, B. E., Pitris, C., Tearney, G. J., Brezinski, M. E., and Fujimoto, J. G. Forward-imaging instruments for optical coherence tomographic imaging. *Opt. Lett.* **22:** 1618, 1997.
18. Thomsen, S. Pathologic analysis of photothermal and photomechanical effects of laser–tissue interactions. *Photochem. Photobiol.* **53:** 825, 1991.
19. LeCarpentier, G. L., Motamedi, M., McMath, L. P., Rastegar, S., and Welch, A. J. Continuous wave laser ablation of tissue: Analysis of thermal and mechanical events. *IEEE Trans. Biomed. Eng.* **40:** 188, 1993.
20. Lin, W-C., Motamedi, M., and Welch, A. J. Dynamics of tissue optics during laser heating of turbid media. *Appl. Opt.* **35:** 3413, 1996.
21. Pettit, G. H., Ediger, M. N., and Weiblinger, R. P. Dynamic optical properties of collagen-based tissue during ArF excimer laser ablation. *Appl. Opt.* **32:** 488, 1993.
22. Toth, C. A., Birngruber, R., Boppart, S. A., Hee, M. R., Fujimoto, J. G., DiCarlo, C. D., Swanson, E. A., Cain, C. P., Narayan, D. G., Noojin, G. D., and Roach, W. P. Argon laser retinal lesions evaluated *in vivo* by optical coherence tomography. *Am. J. Ophthalmol.* **123:** 188, 1997.
23. de Boer, J. F., Milner, T. E., van Gemert, M. J. C., and Nelson, J. S. Two-dimensional birefringence imaging in biological tissue by polarization-sensitive optical coherence tomography. *Opt. Lett.* **22:** 934, 1997.
24. Everett, M. J., Schoenenberger, K., Colston, B. W., Jr., and Da Silva, L. B. Birefringence characterization of biological tissue by use of optical coherence tomography. *Opt. Lett.* **23:** 228, 1998.
25. Ben-Shachar, G., Sivakoff, M. C., Bernard, S. L., Dahms, B. B., and Riemenschneider, T. A. Acute continuous argon-laser induced tissue effects in the isolated canine heart. *Am. Heart J.* **110:** 65, 1985.
26. Profio, A. E., and Doiron, D. R. Transport of light in tissue in photodynamic therapy of cancer. *Photochem. Photobiol.* **46:** 591, 1987.
27. Clivaz, X., Marquis-Weible, F., and Salathe, R. P. Optical low coherence reflectometry with 1.9 μm spatial resolution. *Elec. Lett.* **28:** 1553, 1992.
28. Bouma, B. E., Tearney, G. J., Boppart, S. A., Hee, M. R., Brezinski, M. E., and Fujimoto, J. G. High resolution optical coherence tomographic imaging using a mode-locked Ti:Al_2O_3 laser. *Opt. Lett.* **20:** 1486, 1995.
29. Boppart, S. A., Brezinski, M. E., Pitris, C., and Fujimoto, J. G. Optical coherence tomography for neurosurgical imaging of human intracortical melanoma. *Neurosurgery* **43:** 834, 1998.
30. Herrmann, J. M., Brezinski, M. E., Bouma, B. E., Boppart, S. A., Pitris, C., Southern, J. F., and Fujimoto, J. G. Two- and three-dimensional high-resolution imaging of the human oviduct with optical coherence tomography. *Fertil. Steril.* **70:** 155, 1998.